JTTEE5 8:399-404

The Corrosion Behavior and Microstructure of High-Velocity Oxy-Fuel Sprayed Nickel-Base Amorphous/Nanocrystalline Coatings

A.H. Dent, A.J. Horlock, D.G. McCartney, and S.J. Harris

(Submitted 13 July 1998; in revised form 3 February 1999)

The corrosion characteristics of two Ni-Cr-Mo-B alloy powders sprayed by the high-velocity oxy-fuel (HVOF) process have been studied using potentiodynamic and potentiostatic corrosion analysis in 0.5 *M* H_2SO_4. The deposits were also microstructurally characterized using x-ray diffraction (XRD), scanning electron microscopy (SEM) (utilizing both secondary electron and backscattered electron modes), and transmission electron microscopy (TEM). Results from the microstructural examination of the two alloys have revealed a predominantly amorphous/nanocrystalline face centered cubic (fcc) matrix containing submicron boride precipitates as well as regions of martensitically transformed laths.

Apparent recrystallization of the amorphous matrix has also been observed in the form of cellular crystals with a fcc structure. The oxide stringers observed at splat boundaries were found to be columnar grained α-Cr_2O_3, though regions of the spinel oxide $NiCr_2O_4$ with a globular morphology were also observed. The coatings of the two alloys exhibited comparable resistance to corrosion in 0.5 *M* H_2SO_4, as revealed by potentiodynamic tests. They both had rest potentials approximately equal to –300 mV saturated calomel electrode (SCE) and passive region current densities of ~1 mA/cm^2. Microstructural examination of samples tested potentiostatically revealed the prevalence of degradation at splat boundaries, especially those where significant oxidation of the deposit occurred.

Keywords amorphous, corrosion behavior, microstructural characterization, nanocrystalline, nickel-base

1. Introduction

High-velocity oxy-fuel (HVOF) thermal spraying has been widely used to deposit low porosity, wear resistant cermet coatings based on materials such as WC-Co. In recent years the process has been extended to deposit metallic coatings with low porosity for corrosion resistant applications, using alloys such as Inconel 625 (Ref 1, 2). There are now, however, growing demands for the deposition of coatings with good corrosion resistance combined with high hardness and wear resistance. Several authors (Ref 3-5) have demonstrated that both high hardness (~1000 kgf/mm^2) and excellent corrosion resistance can be achieved in iron or nickel-base alloys containing metalloid elements such as boron when melt spun to form ribbons in which the high cooling rate of ~10^6 K/s leads to an amorphous structure being formed. Thus, this class of material should be attractive for deposition by thermal spraying in which similarly high cooling rates can be attained.

Only a limited amount of work has been done on the production and properties of air and vacuum plasma sprayed amorphous/nanocrystalline NiCrB and FeCrB based alloys (Ref 3, 6-10), but the work has demonstrated that excellent wear and corrosion resistance is possible. However, the existence of features such as splat boundaries and oxides within thermally sprayed coatings necessitates a detailed and specific study of HVOF deposits, particularly with regard to their ability to protect against aggressive environments as demonstrated (Ref 11) for HVOF sprayed FeCrB base alloys.

The purpose of the present article is to report the results of producing HVOF sprayed coatings of two experimental NiCrMoB alloys using hydrogen as a fuel gas. In this work the influences of alloy composition and HVOF process parameters on phase formation, microstructure development, and the corrosion behavior in 0.5 *M* H_2SO_4 were examined.

2. Experimental Procedures

The two nickel-base alloy powders employed were produced using inert gas (argon) atomization by Phoenix Scientific Industries (Farnborough, U.K.) and sieved to a particle size range of 25 to 63 μm. Table 1 shows the chemically analyzed compositions of the alloys, designated A and B.

Both alloy powders were HVOF sprayed using a Miller thermal spray system (Praxair Surface Technologies, Appleton, WI) with hydrogen as a fuel gas, onto 2 mm thick mild steel coupons grit blasted and cleaned with acetone prior to deposition. The

This paper originally appeared in *Thermal Spray: Meeting the Challenges of the 21st Century; Proceedings of the 15th International Thermal Spray Conference,* C. Coddet, Ed., ASM International, Materials Park, OH, 1998. This proceedings paper has been extensively reviewed according to the editorial policy of the *Journal of Thermal Spray Technology.*

A.H. Dent, A.J. Horlock, D.G. McCartney, and **S.J. Harris,** Department of Materials Engineering and Materials Design, University of Nottingham, University Park, Nottingham, NG7 2RD, U.K. Contact e-mail: graham.mccartney@nott.ac.uk.

samples were mounted on a horizontal turntable and rotated at a surface speed of ~1 m/s, with the HVOF gun being traversed vertically at 5 mm/s. Air jets operating at 6 bar pressure were used to cool the substrates during deposition. The stand-off distance was 250 mm, and the gun was operated with a 19 mm combustion chamber. Table 2 lists the spray parameters, which were varied in the deposition of the powders for this study. Alloys A and B were both deposited using settings labeled 1 and 2 to give four sets of samples designated A1, A2, B1, and B2, respectively. Table 2 presents the spray parameters used to deposit the two alloys.

X-ray diffraction (XRD) of the powders and resultant coatings was undertaken on a diffractometer using copper Kα radiation, a scanning rate of 1.5°/min and a step size of 0.05°. A Jeol 6400 (JEOL (UK) Ltd., Welwyn Garden City) scanning electron microscope (SEM) was employed to examine the corroded surfaces as well as mounted and polished cross sections of the as-sprayed coatings using both the secondary electron (SE) and backscattered electron (BSE) signals. A Jeol 2000FX transmission electron microscope (TEM) was used to investigate the fine structure of the as-sprayed deposits. Thin foils for TEM were prepared from samples taken parallel to the substrate-coating interface. These samples were ground and dimpled prior to final ion beam thinning to electron transparency. The SEM and TEM instruments both incorporated quantitative energy dispersive x-ray (EDX) analysis facilities. Microhardness measurements were performed on coating cross sections using a load of 300 g.

Potentiodynamic corrosion tests of anodically polarized samples of each coating (100 mm^2 surface area) were carried out at a scanning rate of 10 mV/min in accordance with the ASTM G 5-94 standard procedure (Ref 12). The tests were performed both on deposits removed from the substrates and on coatings still adhered to the mild steel coupons. Potentiostatic corrosion tests were also carried out on a number of the coatings from both alloys for periods of up to 600 s. Two voltages were used, a prepassive and a transpassive value; exact voltages were dependent upon the form of the potentiodynamic curve for each particular coating.

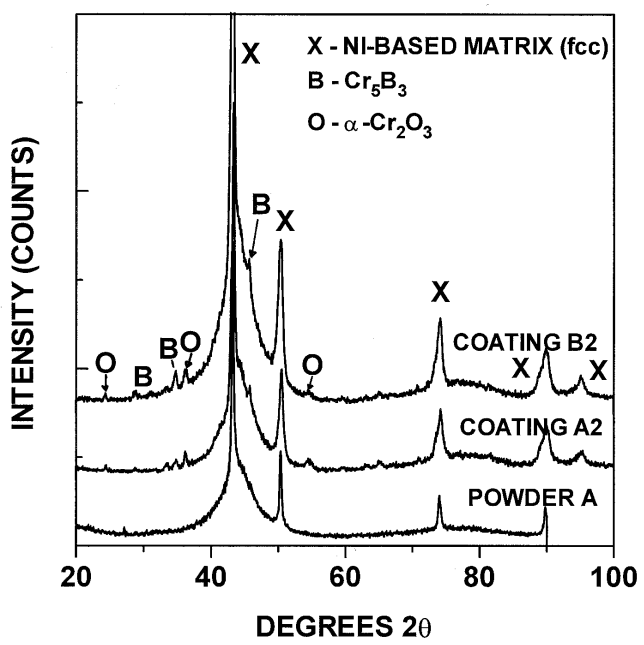

Fig. 1 X-ray diffraction spectra from the as-received powder A and from high-velocity oxy-fuel sprayed coatings A2 and B2

3. Results

3.1 Microstructural Characterization

X-ray diffraction indicated that the as-received powders both had predominantly cubic-F structures, and SEM showed spherical powder morphologies consistent with inert gas atomization. X-ray diffraction scans of powder A and coatings obtained from A and B under spray condition 2 (labeled A2 and B2, respectively) are shown in Fig. 1. It is clear that A2 and B2 also exhibit predominantly crystalline fcc matrices as indicated by the peaks marked X. There is, in addition, evidence for α-Cr_2O_3 and Cr_5B_3 in both coatings as seen from peaks labeled O and B, respectively. The significant broadening of the fcc nickel peak at $2\theta \cong 44°$ indicates the presence of amorphous material within both the powder and the deposits. The XRD spectra from powder B and coatings A1 and B1 were broadly similar, respectively, to those shown in Fig. 1.

Estimates for the relative oxide contents of the materials were obtained from the ratio of the intensities of the α-Cr_2O_3

Table 1 Compositions of alloy powders A and B as obtained by chemical analysis

	Alloy A		Alloy B	
Element	wt%	at.%	wt%	at.%
Ni	56	55	50.6	50
Cr	22.5	25	22.5	25
Mo	20	12	25	15
B	1.5	8	1.9	10

Table 2 Spray parameter settings used in the deposition

	Parameter value	
Spray parameter	Setting 1	Setting 2
Total gas flow, NL/min	980	915
Oxygen flow, NL/min	245	240
Hydrogen flow, NL/min	735	675
H_2 to O_2 gas ratio	3 to 1	2.8 to 1
Powder feed rate, kg/h	~1.9	~1.9

Table 3 X-ray diffraction intensity ratios in different samples

Material	Oxide: Matrix peak ratio
A	
Powder	0.048
Coating A1	0.105
Coating A2	0.093
B	
Powder	0.054
Coating B1	0.107
Coating B2	0.105

peak at $2\theta \cong 36.5°$ to the {111} nickel fcc peak at $2\theta \cong 44°$. These values are listed in Table 3, and it is clear that the oxide contents of the coatings were somewhat higher than those of the starting powders. However, the oxide contents of A and B were similar and depended little on whether conditions 1 or 2 were used. The microstructure of the as-sprayed coating, for all the samples observed, appeared to be of low porosity and well bonded to the substrate. A BSE image of a typical cross section is shown in Fig. 2. This reveals a splatlike morphology typical of thermally sprayed deposits, although a small number of near-spherical unmelted particles are also visible. The splats themselves appeared to exhibit one of the two types of contrast visible in Fig. 2. Energy dispersive x-ray analysis did not reveal significant composition differences between splats of different contrast. However, similar contrast differences were also noted on powder particle cross sections imaged using the BSE signal, with smaller particles and the mantles of larger particles exhibiting the lighter contrast. This could suggest that the lighter areas were amorphous and the darker regions crystalline in both powders and coatings. In addition layers of oxide were observed at intersplat boundaries, as confirmed by EDX analysis.

The plan view TEM investigation of the alloy coatings revealed a predominantly nanocrystalline/amorphous matrix though regions of microcrystallinity (grain sizes of the order of 0.2 to 1 μm) were also observed. Figure 3 is a TEM micrograph of a plan view of coating B1 and shows the amorphous and crystalline regions separated by a splat boundary. The inset diffraction pattern from both areas comprises a diffuse amorphous diffraction ring as well as rings of discrete spots from fine grained crystalline material. Some areas of the matrix were noted to have formed martensitic-type, highly faulted 10 to 50 nm wide laths up to 500 nm in length, while cellular-type grains 100 to 500 nm in size, with a nickel-base fcc structure, were also found within amorphous regions. Figure 4 shows the latter feature.

Boride precipitates in the size range 10 to 50 nm, corresponding to the Cr_5B_3 phase identified by XRD analysis (see Fig. 1), were found embedded within both the amorphous and nanocrystalline regions of the metallic matrix, whereas stringers of α-Cr_2O_3 were present predominantly at intersplat boundaries as shown in the TEM image of Fig. 5. Globular spinel oxide crystals, $NiCr_2O_4$, were also observable, but the absence of these spinel peaks from the XRD spectra suggests that their overall percentage was <3%.

Coatings of A1 and A2 had average hardnesses, from ten measurements, of 610 and 710 ± 10 kgf/mm^2, respectively, whereas B1 and B2 were significantly harder with values of 745 and 810 ± 15 kgf/mm^2, respectively.

3.2 Corrosion Testing

Anodic polarization curves representative of the thermally sprayed coatings from alloys A and B are shown in Fig. 6 as the curves labeled 1 and 2, respectively. The corrosion potentials of the coatings were similar at approximately –280 mV relative to the saturated calomel electrode (SCE). They exhibited similar current densities (≅2 mA/cm^2) in the passive region and the

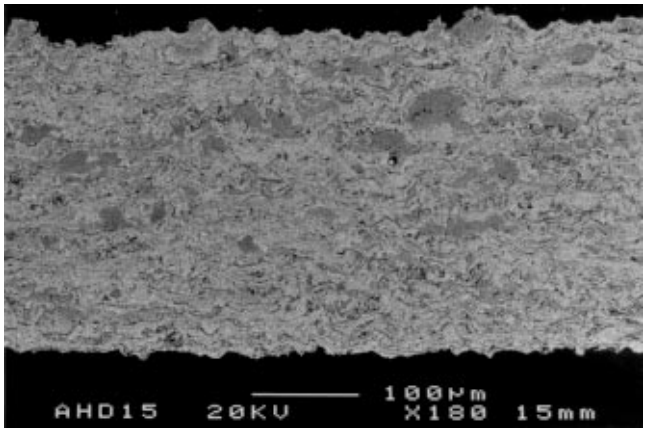

Fig. 2 Back scattered electron micrograph of high-velocity oxy-fuel sprayed coating A1 showing a characteristic, splatlike layered morphology together with isolated, near-spherical unmelted particles. Two different contrast levels of the metallic matrix are also apparent.

Fig. 3 Transmission electron micrograph of a typical region of coating B1 showing amorphous and nanocrystalline regions with a splat boundary separating them. The inset diffraction pattern, showing amorphous and polycrystalline ring patterns, is from the entire region.

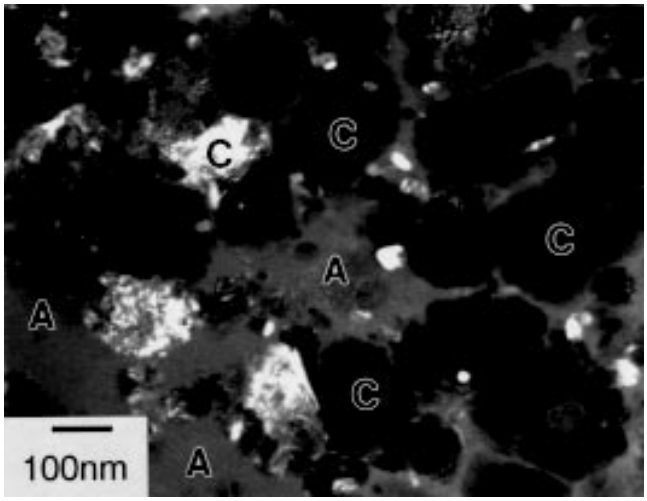

Fig. 4 Dark field transmission electron microscope image of crystalline cellular crystals (C) within an amorphous matrix (A)

onset of transpassive behavior occurred at around +900 mV SCE. The coatings from alloy powder B, with the higher molybdenum and boron contents, are seen to have, however, a more pronounced two stage passivation behavior than those from powder A. For comparison the polarization curves for a HVOF sprayed coating of Inconel 625 and wrought Inconel 625 are also shown in Fig. 6, by plots 3 and 4, respectively. The wrought Inconel displays a low passive current density of around 10 $\mu A/cm^2$, as expected; whereas the passive current densities of the three coatings are similar at ~2 mA cm^2. Transpassive behavior is observed in all materials at similar anodic potentials of around 900 mV (SCE), and all exhibit similar corrosion potentials of around –300 mV (SCE).

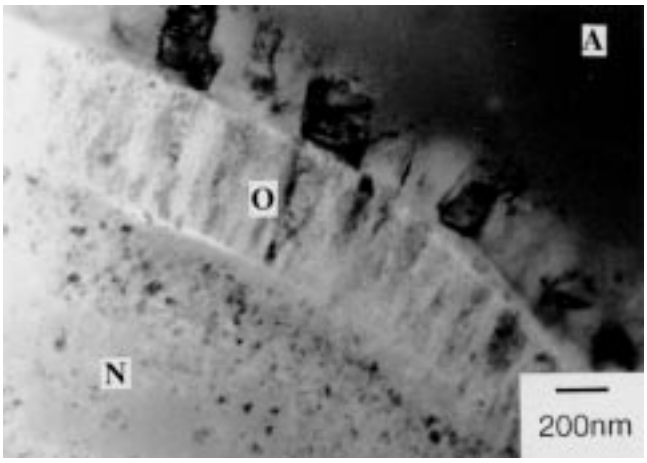

Fig. 5 Transmission electron microscope image of coating B2 showing a layer of columnar-grained α-Cr_2O_3 (O) separating amorphous (A) and nanocrystalline (N) metallic matrix regions

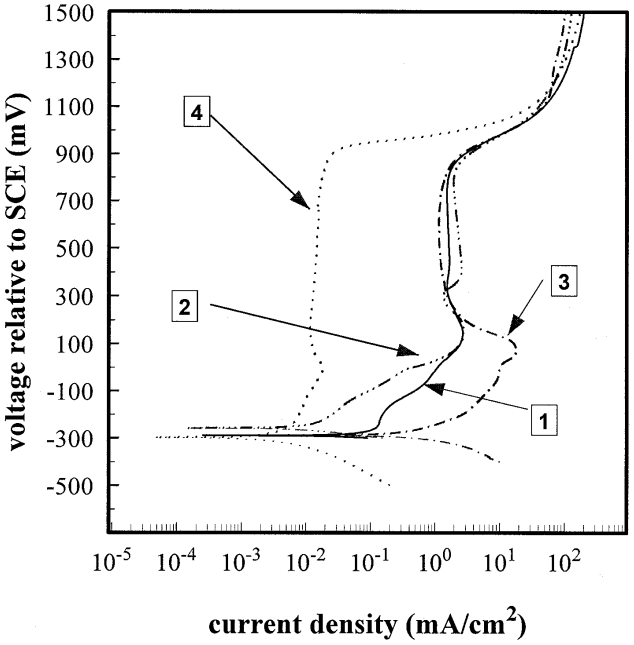

Fig. 6 Anodic polarization curves in 0.5 *M* H_2SO_4 for high-velocity oxy-fuel sprayed coatings of alloy A (1), alloy B (2), Inconel 625 (3), and wrought Inconel 625 (4)

It was found that the polarization curves obtained from coatings that had been removed from their mild steel substrates were of an identical form to those displayed in Fig. 6. Furthermore, the values of corrosion potential, passive current density, and the potential for the onset of transpassive corrosion were broadly similar to those obtained from adherent coatings, thus indicating that the substrate was not influencing the behavior in the potentiodynamic tests.

In the potentiostatic tests on coatings from powders A and B two different types of attack were observed to take place depending on whether the sample was anodically polarized into the passive or transpassive region. In the passive region attack was predominately around intersplat boundaries, as shown in the SE image of the corroded surface of coating B2 seen in Fig. 7. Here it is apparent that there are relatively deep corrosion furrows along splat boundaries, whereas the central regions of splats still exhibit 1200 grit grinding scratches arising from sample preparation. In the transpassive region a much more general form of attack occurred in which both splats and splat boundaries were severely corroded.

4. Discussion

The development of a layered microstructure in these HVOF sprayed coatings is typical for metallic alloys. The formation of the Cr_2O_3 phase at intersplat boundaries is also to be expected for a number of reasons, even though the fuel to oxygen ratio was only around 67% of the stoichiometric requirement (see Table 2). First, there is a small concentration of unreacted oxygen within the spray gun because of nonequilibrium combustion conditions. Secondly, molten alloy particles are inevitably exposed to air, entrained into the hot gas free jet, and thirdly, oxidation can also occur at the exposed surface of splats, solidified on the substrate, prior to deposition of a subsequent layer. However, the susceptibility to oxidation does not appear to depend on alloy composition for the powders examined and, for the spray conditions reported, process parameters also had little effect.

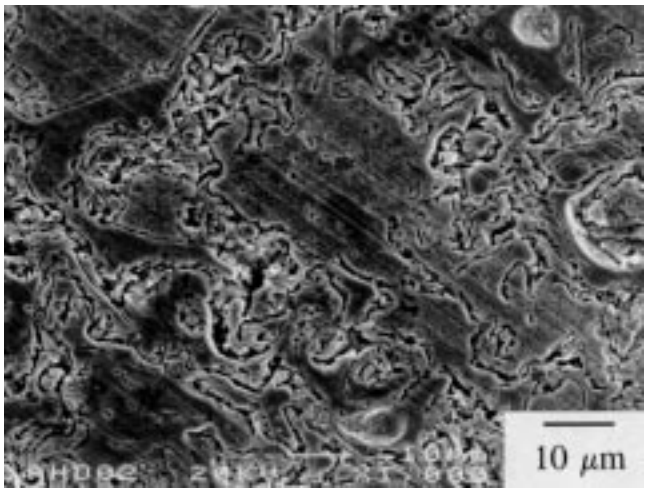

Fig. 7 Secondary electron micrograph of the surface of coating A2 potentiostatically corroded in 0.5 *M* H_2SO_4 at +400 mV saturated calomel electrode. The retained grinding marks in intrasplat regions and deep furrows at intersplat boundaries are visible.

The diffuse diffraction haloes in the XRD spectrum of Fig. 1 are indicative of some fraction of amorphous structure in the coating and has been confirmed by the plan view TEM study. Indeed, the TEM work has revealed that the coating structures are far from homogeneous with a range of microstructural features including Cr_5B_3, Cr_2O_3, and $NiCr_2O_4$ in addition to the principal nickel-base amorphous/crystalline matrix. This inhomogeneous, partly amorphous structure is entirely consistent with previous studies on alloys of similar compositions, although plasma sprayed, by Sampath et al. (Ref 6) and Das et al. (Ref 3). A possible explanation of the mixed crystalline/amorphous matrix structure is the different cooling rates experienced by different splats or even regions within single splats. The reheating of splats by the deposition of subsequent layers could also promote solid state crystallization of material, which formed initially with an amorphous structure. It is also not clear whether borides formed directly from the melt or through a solid state precipitation reaction. Further investigations are underway.

The effect of increasing the amounts of molybdenum and boron present in the feedstock powder (and hence coating) was to increase significantly the deposit microhardness from around 660 kgf/mm^2 for coatings from powder A to around 770 kgf/mm^2 for coatings from powder B.

With regard to the corrosion properties, it is important to emphasize that the behavior of coatings adhered to mild steel substrates was identical to those removed from the substrates. This indicates that the deposits were dense and continuous and that there was not a path for the sulfuric acid to permeate to the mild steel base material. Siitonen et al. (Ref 13) have, by contrast, observed marked differences between free standing coatings and coatings on substrates when significant connected porosity was present.

It is apparent from Fig. 6 (plots 1 and 2) that the molybdenum and boron content of the deposit, over the range studied, only influenced the prepassivation corrosion behavior. The higher molybdenum and boron coatings (from alloy B) had significantly lower current densities when polarized to between –100 and +100 mV (SCE) than did the lower molybdenum and boron coatings (from alloy A). Das et al. (Ref 3) observed similar features in anodically polarized melt spun ribbons of NiCrMoB alloys of compositions close to those used in the current study. However, the passivation current densities of these melt spun ribbons containing 20 to 25 at.% Cr were of the order of 10 μA/cm^2 compared to the values of around 10^3 μA/cm^2 for the present deposits. It is believed that preferential attack at intersplat boundaries, as evidenced in Fig. 7, is responsible for the much higher current densities in sprayed deposits. This is confirmed by the comparisons between HVOF-sprayed and wrought Inconel 625 shown by plots 3 and 4 in Fig. 6. The passivation current density values for the NiCrMoB coatings in this study are, nevertheless, comparable to that for sprayed Inconel and those reported previously by Kishitake et al. (Ref 8) and Dent et al. (Ref 11) for the corrosion of thermally sprayed iron-chromium based amorphous coatings in 0.5 *M* H_2SO_4. It seems probable, therefore, that the oxidation of particles/splats during spraying must be significantly reduced in order to achieve a lowering of the passivation current density in thermally sprayed coatings. Work is continuing to achieve this.

5. Conclusions

The following conclusions can be drawn:

- High-velocity oxy-fuel spraying was employed to successfully deposit coatings of two different NiCrMoB alloys with substantially amorphous/nanocrystalline matrices and hardness values in excess of 610 ± 10 kgf/mm^2. Higher molybdenum and boron levels led to higher hardness values of up to 810 ± 15 kgf/mm^2.
- The deposited layers were found to contain fine Cr_5B_3 precipitates within the metallic matrix phase. The predominant oxide phase, Cr_2O_3, occurred principally with a columnar grained morphology at intersplat boundaries.
- Anodic polarization curves showed that in 0.5 *M* H_2SO_4 a passive region occurred between approximately +100 and +900 mV (SCE). Increased molybdenum and boron levels modified the prepassivation corrosion current density but had little effect on either passive current density or the onset of transpassive corrosion.
- The potentiodynamic corrosion testing also demonstrated that the corrosion behavior of the experimental coatings A and B was similar to that of HVOF sprayed Inconel 625. However, the presence of oxides at intersplat boundaries leads to passive current densities higher than those observed in wrought alloys or melt spun ribbons.

Acknowledgments

The authors acknowledge financial support from the Engineering and Physical Sciences Research Council through the award of a ROPA grant (GR/K/63993). They are also grateful to Professor J.V. Wood for the provision of laboratory facilities.

References

1. P.E. Arvidsson, Comparison of Superalloy Coatings Sprayed with Plasma and HVOF, *Thermal Spray Coatings: Properties, Processes and Applications*, T.F. Bernecki, Ed., ASM International, 1991, p 295-301
2. H. Edris, D.G. McCartney, and A.J. Sturgeon, Microstructural Characterization of High Velocity Oxy-Fuel Sprayed Coatings of Inconel 625, *J. Mater. Sci.*, Vol 32, 1997, p 863-872
3. S.K. Das, E.M. Norin, and R.L. Bye, Ni-Mo-Cr-B Alloys: Corrosion Resistant Amorphous Hardfacing Coatings, *Mater. Res. Soc. Symp. Proc.*, Vol 28, B.H. Kear and M. Cohen, Ed., Elsevier Science Publishing Co., 1984, p 233-237
4. R. Ray, Hot Consolidation/Devitrification of Metallic Glasses, *Rapidly Solidified Amorphous and Crystalline Alloys*, B.H. Kear, B.C. Giessen, and M. Cohen, Ed., Elsevier Science Publishing Co., 1982
5. W.L. Johnson, Metallic Glasses, *ASM Metals Handbook*, Vol 2, *Properties and Selection: Nonferrous Alloys and Special-Purpose Materials*, ASM International, 1990, p 804-821
6. S. Sampath, R.A. Neiser, H. Herman, J.P. Kirkland, and W.T. Elam, A Structural Investigation of a Plasma Sprayed Ni-Cr Based Alloy Coating, *J. Mater. Res.*, Vol 8 (No. 1), 1993, p 78-86
7. V. Panchanathan, C.L. Tsai, and S. Wang, Nickel Base Metallic Glass Powders for Applications as Plasma Sprayed Coatings, *Rapidly Solidified Amorphous and Crystalline Alloys*, B.H. Kear, B.C. Giessen, and M. Cohen, Ed., Elsevier Science Publishing Co., 1982
8. K. Kishitake, H. Era, and F. Otsubo, Characterization of Plasma Sprayed Fe-10Cr-10Mo-(C, B) Amorphous Coatings, *J. Therm. Spray Technol.*, Vol 5 (No. 2), 1996, p 145-153

9. K. Kishitake, H. Era, and F. Otsubo, Characterization of Plasma Sprayed Fe-17Cr-38Mo-4C Amorphous Coatings Crystallizing at Extremely High Temperature, *J. Therm. Spray Technol.*, Vol 5 (No. 3), 1996, p 283-288
10. T. Shmyreva, A. Mukhin, and L. Mukhina, Detonation Gun and Plasma Spraying of Amorphous Metal Coatings with Improved Corrosion Resistance, *Thermal Spray Science and Technology*, C.C. Berndt and S. Sampath, Ed., ASM International, 1995, p 243-247
11. A.H. Dent, A.J. Horlock, D.G. McCartney, and S.J. Harris, The Structure and Properties of Two Fe-Cr-B Based Coatings Sprayed Using HVOF, *Thermal Spray: A United Forum for Scientific and Technological Advances*, C.C. Berndt, Ed., ASM International, 1997, p 917-923
12. ASTM Designation G 5-94, *Annual Book of ASTM Standards*, ASTM, 1994, p 48-58
13. P. Siitonen, S.L. Chen, K. Niemi, and P. Vuoristo, Electrochemical Method for Evaluating the Corrosion Resistance and Porosity of Thermal Sprayed Coatings, *Thermal Spray: International Advances in Coatings Technology*, C.C. Berndt, Ed., ASM International, 1992, p 853-858